Contents lists available at ScienceDirect

Applied Catalysis B: Environmental

On the mechanism of visible-light accelerated methane dry reforming reaction over Ni/CeO$_{2-x}$ catalysts

Kristijan Lorber [a,c], Janez Zavašnik [b], Jordi Sancho-Parramon [d], Matej Bubaš [d], Matjaž Mazaj [a], Petar Djinović [a,c,*]

[a] Department of Inorganic Chemistry and Technology, National Institute of Chemistry, Hajdrihova 19, SI-1000 Ljubljana, Slovenia
[b] Jožef Stefan Institute, Jamova cesta 39, SI-1000 Ljubljana, Slovenia
[c] University of Nova Gorica, Vipavska 13, SI-5000 Nova Gorica, Slovenia
[d] Ruđer Bošković Institute, Division of Materials Physics, Bijenička cesta 54, 10000 Zagreb, Croatia

ARTICLE INFO

ABSTRACT

The methane dry reforming reaction (DRM) converts methane and CO$_2$ into syngas, a mixture of H$_2$ and CO. When illuminated by 790 mW cm^{-2} of white light, the 2Ni/CeO$_{2-x}$ catalyst converts CH$_4$ and CO$_2$ beyond thermodynamic equilibrium, while the energy efficiency reaches 33%. The DRM reaction is sustained in a purely photocatalytic mode without external heating, yielding CH$_4$ and CO$_2$ rates of 0.21 and 0.75 mmol (g$_{cat}$ • min)$^{-1}$, respectively. Theoretical analysis of Ni/CeO$_{2-x}$ optical properties agrees with *in-situ* UV-Vis DRS results and reveals partly reduced Ce^{3+} sites crucial for extending the optical absorption of Ni/CeO$_{2-x}$ into the visible light range. Two photocatalytic mechanisms are postulated to occur: the hot charge-carrier driven photocatalytic mechanism and the near-field induced resonant energy transfer, depending on the energy of photons used to stimulate the catalyst. This work identifies sub-stoichiometric Ni/CeO$_{2-x}$ as highly efficient for boosting methane activation by visible light under mild conditions.

1. Introduction

Methane dry reforming reaction (DRM, CH$_4$ + CO$_2$ ↔ 2CO + 2H$_2$) represents an attractive pathway for converting methane (an abundant and cheap hydrocarbon) and CO$_2$ (greenhouse gas) into a mixture of H$_2$ and CO (syngas). DRM is among few catalytic CO$_2$ reduction processes (such as CO$_2$ hydrogenation to methanol, reverse water gas shift and Sabatier reaction), which could be implemented on a global megaton scale to mitigate anthropogenic CO$_2$ emissions, and thus minimize their impact on climate change [1–3]. Syngas is widely used in the petrochemical industry for synfuel production *via* the Fischer-Tropsch process, as well as for hydrogenation, hydroformylation and carbonylation reactions [4]. The downsides of the DRM reaction are high endothermicity (ΔH_r = 247 kJ mol^{-1}, $\Delta G_{298\ K}$ = 171 kJ mol^{-1}) and unfavorable thermodynamic equilibrium values at low reaction temperatures, which limit achievable conversion and hydrogen selectivity. The DRM reaction has been extensively studied at high temperatures (> 600 °C) over transition (Ni, Co and Fe), as well as noble metal catalysts (Ru, Rh, Pt and Pd) [5]. Nickel exhibits high activity for

methane activation [6] and when dispersed in the form of nanoparticles over CeO$_2$, yields an affordable and outstandingly active DRM catalyst [7,8]. Also, if the nickel cluster size is maintained below 5 nm, carbon accumulation during the reaction can be avoided [9], which overcomes a substantial hurdle in the industrial application of this reaction [5]. Abundance of oxygen vacancies on ceria, manifested through its redox activity [10], is regarded crucial for kinetic balancing of carbon accumulation and gasification reactions during DRM, preventing carbon accumulation on catalysts and consequent deactivation [11,12]. In the past years, catalysis over nano-shaped ceria revealed notable improvements of activity in several reduction and oxidation reactions [13], which appear to be correlated with ease of oxygen vacancy formation over its different terminating facets [13,14]. Activity dependence on ceria shape was also observed in DRM reaction over Ni/CeO$_2$ catalysts [15].

Photocatalysis is a promising pathway for converting intermittent light (photon energy) into storable chemical energy [16–18]. Illumination of the catalyst can significantly accelerate the reaction rates, and conversions beyond the thermodynamic equilibrium can be achieved

---

due to non-thermal, vibrational and electronic stimulation of adsorbed reactants and reaction intermediates [19,20]. Thus, (photo)catalytic reactions can be performed at lower temperatures and pressures, which is often beneficial in terms of product selectivity, catalyst stability as well as process cost and design.

Several works investigating plasmonic and non-plasmonic metals (Au, Pd, Pt and Rh) supported on black titania, Al_2O_3, TaON, Ta_3N_5 and SiO_2 report increased H_2 and CO yields during photocatalytic, compared to thermocatalytic DRM reaction [21–24]. Shoji et al. [19]. report that $Rh/SrTiO_3$ catalyst enables methane and CO_2 conversions far beyond thermodynamic equilibrium under UV-light irradiation and without additional heating. The photocatalytically produced syngas contained an equimolar H_2 and CO content, which is not achievable during thermocatalytic DRM reaction due to the large fraction of hydrogen being converted to water by the kinetically dominant RWGS reaction [25].

Halas et al. [26]. utilized plasmonic Cu antennas decorated with Ru single sites, which enabled up to a 5-fold increase of methane reaction rate compared to thermocatalysis, and 100% H_2 selectivity when the catalyst was illuminated by > 16 W cm^{-2} of white light.

It is becoming clear that visible and UV light have a notable benefit on catalytic activity and selectivity in DRM reaction over noble metals (Rh [19], Au [21,23], Pt [22], Pd [23] and Ru [26]). From an academic, industrial, and practical perspective, a strong photocatalytic response in DRM reaction over transition metal/semiconductor photocatalysts that can be produced with a scalable synthesis method is highly desired.

This work investigates the applicability of Ni/CeO_{2-x} nanorod catalyst for visible-light driven DRM reaction at mild conditions and analyzes the underlying reaction mechanisms. The *in-situ* UV-Vis DRS analysis showed facile catalyst activation by visible light, confirmed by simulation of its electromagnetic properties. The consequences of catalyst illumination by 790 mW cm^{-2} of white light ($400 < \lambda < 700$ nm) were up to an 8.5-fold increase in methane rate and improved H_2 selectivity (H_2/CO increased from 0.23 to 0.59) compared to thermocatalytic DRM at a constant catalyst temperature of 400 °C. Also, CH_4 and CO_2 conversions beyond the thermodynamic equilibrium were achievable at temperatures below 250 and 300 °C, respectively.

2. Experimental section

2.1. Material synthesis

The selection of ceria nanorod morphology as the catalyst support is based on our preliminary screening of nickel on ceria nanorod and nanocube catalysts (Fig. S1). The nanorod based catalyst was more active, accumulated far less carbon and maintained a higher fraction of Ce^{3+}, which is important for visible light absorption [27]. The CeO_2 nanorods were synthesized according to Zabilskiy et al. [28] by dissolving 53.8 g of NaOH (99% purity, Merck) in 140 ml of ultrapure water. Then, 84 ml of the aqueous solution containing 4.9 g of Ce $(NO_3)_3 \cdot 6H_2O$ (99% purity, Sigma-Aldrich) was added under vigorous stirring. The suspension was stirred for additional 30 min and transferred into Teflon® lined stainless steel autoclaves (volume $\sim$ 35 ml each), where it was aged for 24 h at 100 °C in a laboratory drier. After autoclave quenching, the suspension was filtered, freeze dried overnight and calcined in air (4 h at 500 °C, heating ramp of 5 °C min^{-1}, Nabertherm P330).

Different nickel loadings (0.5, 1, 2 and 4 wt% nominal) were deposited by adding 2.5% NH_4OH solution to the aqueous suspension containing CeO_2 nanorods and an appropriate amount of dissolved Ni $(NO_3)_2$ (Sigma Aldrich, purity 99%), until pH reached 7.7. After 2 h of stirring, the pH of the suspension was raised to 9.5 using 25% NH_4OH and stirred for an additional 30 min. The efficiency of nickel deposition was verified spectrophotometrically by analyzing the mother liquor using a Spectroquant® NOVA60 analyzer (Merck). In all cases, the efficiency of nickel deposition was above 98%, and nominal loadings were considered actual. Finally, the suspension was filtered, dried overnight

at 70 °C in a laboratory drier, and calcined in air for 4 h at 500 °C (Nabertherm P330). The samples are denoted as CeO_2-R for the bare ceria support and xNi for nickel ceria nanorod catalysts, where "x" represents the nickel loading.

2.2. Characterization

The *in-situ* UV-Vis DRS analysis was performed on the Lambda 650 apparatus (Perkin Elmer) equipped with a HVC-VUV-5 reaction chamber from Harrick. Finely powdered samples ($\sim$ 10 mg) were analyzed in air at 25 °C and in 5% H_2/N_2 (flow of 10 ml min^{-1}, purity 5.0 by Messer) after dwelling the sample at 200 and 450 °C for 30 min. Spectralon® white standard was used to record the background.

The XRD analyses were performed on a Panalytical XP PRO MPD apparatus using $Cu_{\alpha1}$ irradiation ($\lambda = 1.5406$ Å) in the 2theta range between 10° and 80°, step size of 0.034° and fully opened 100 channel X′Celerator detector.

The H_2 adsorption experiments were performed on a IMI-HTP manometric sorption analyzer (Hiden Isochema Inc.). Prior the isothermal measurements, the catalyst samples were reduced *in-situ* in pure H_2 flow of 10 ml min^{-1} while ramping the reactor temperature at 5 °C min^{-1} to 350 °C. After the reduction pretreatment lasting 16 h, the sorption isotherms were measured at 110 °C in the pressure range between 50 and 1000 mbar. The chemisorbed H_2 values were estimated from extrapolating the linear part of the H_2 desorption isotherm to zero pressure as described by Słowik et al. [29] and the average nickel particle size was adopted from Velu et al. [30].

The N_2 physisorption technique (Tristar II apparatus from Micromeritics) was used to analyze BET specific surface area, total pore volume and average pore size (BJH method) of the synthesized catalysts. Before analysis, the samples were degassed 1 h at 90 °C, followed by 4 h at 300 °C in N_2 flow (purity 6.0, Linde) on a SmartPrep accessory (Micromeritics).

Thermogravimetric analysis (TGA) was used to quantify carbon accumulated on the catalyst during the reaction. The samples were heated in airflow (25 ml min^{-1}) from 50 to 800 °C with a 10 °C min^{-1} ramp (Perkin Elmer, model STA6000). Carbon mass was calculated from the mass difference before and after analysis.

H_2-temperature programmed reduction (H_2-TPR) was performed on an AutoChem 2920 apparatus to analyze the reduction of materials and quantify the amount of consumed H_2. Before analysis, the samples were *in-situ* pretreated in synthetic air at 300 °C for 15 min. After cooling to 10 °C, the atmosphere was changed to 5% H_2/Ar (25 ml min^{-1}), and a temperature ramp of 10 °C min^{-1} was used to heat the sample (100 mg) to the final temperature of 550 °C. H_2 consumption was analyzed with a TCD detector, and a LN_2/isopropanol cold trap was used to remove water vapor and eliminate its contribution to H_2 quantification.

For TEM analyses, powder samples were first dispersed in absolute ethanol and sonicated to prevent agglomeration of the nanoparticles. Such prepared suspension was transferred onto commercial lacey-carbon Cu support grids. TEM analyses (conventional TEM micrographs, HR-TEM and electron diffraction patterns) were performed on a LaB_6 JEM-2100 microscope (Jeol Inc.), operated at 200 kV and additionally equipped with an energy-dispersive X-ray spectrometer (EDS, model EX-24063JGT, Jeol Inc.). TEM micrographs were recorded by Orius SCD-1000 (Gatan Inc.) slow-scan CCD camera.

Simulation of electromagnetic properties of bare CeO_2 rods, spherical Ni particles and Ni/CeO_2 nanorod catalysts was done using the MNPBEM implementation of the boundary element method [31]. Optical constants for Ni, oxidized and reduced ceria were taken from literature [32,33]. In all calculations, the CeO_2 rods are assumed to be in an air-like environment. Calculations were done averaging over different light polarization directions with respect to the rod axis to simulate a random orientation of nanorods.

2.3. Catalytic experimentation

Catalytic tests were performed in a modified reaction chamber (HVC-MRA-5, Harrick, Figs. S2 and S3) between 180 and 470 °C. During thermo-catalytic experiments, the catalyst temperature was varied in 10–50 °C increments by changing the power output of the electric heater. During light-assisted experiments, the catalysts were illuminated by 790 mW cm^{-2} of white light, and the catalyst temperature was varied by changing the power output of the electric heater. Schott KL2500 LED source (400 $< \lambda <$ 700 nm, Fig. S4) was used for catalyst illumination, equipped with an optic fiber having a 9 mm active diameter and light focusing lenses (Thorlabs Inc.), which concentrated the light to a spot equal to the catalyst pellet diameter (4.5 mm) with a maximum intensity of 790 mW cm^{-2} (measured by Thorlabs PM100D photometer). For all tests, 2 mg of finely powdered catalyst was used, which formed a round pellet measuring 4.5 mm in diameter and 0.5 mm in thickness. The catalyst was positioned on top of a 1 mm thick layer of powdered SiC (Sicat, 30–150 μm) to improve heat transfer from the furnace to the sample and minimize radial temperature gradient in the catalyst layer. The catalyst temperature was measured with a 0.25 mm O.D. thermo-couple (Omega Engineering Inc., model SCASS-010U-12) just pene-trating the catalyst bed from the bottom with the tip located about 0.2 mm below the illuminated catalytic surface. Before reaction, the catalysts were activated *in-situ* in a 10 ml min^{-1} flow of 5% H$_2$/N$_2$ (Messer, purity 5.0) at 470 °C for 30 min. For the catalytic reactions, the atmosphere was switched to equimolar flow of CH$_4$ and CO$_2$ (Linde, purity 5.0 and 5.3, respectively, 10 ml min^{-1} each, without any dilution, WHSV = 600 L(g$_{cat}$ • h)$^{-1}$). The equimolar CH$_4$-CO$_2$ feed was used in all experiments, in accordance with the stoichiometry of the DRM reaction.

All catalytic tests were performed in the kinetic regime to ensure intrinsic activities are reported. Analysis of gas leaving the photo-catalytic reactor was performed by GC (model 490, equipped with MS5A and PPU columns by Agilent). Each reported activity point is a calcu-lated average of at least five analytical repetitions.

3. Results

3.1. Catalyst characterization

The specific surface area of CeO$_2$-R with the value of 84 m^2 g^{-1} changed negligibly after the nickel deposition, regardless of its loading (0.5–4 wt% of Ni). The average pore size determined by BJH method defining interparticle porosity was found to be 11 nm for bare CeO$_2$-R and increased slightly for the Ni/CeO$_2$ catalysts (13–16 nm, Table S1).

The XRD analysis (Fig. S5) confirmed the presence of the Face Centered Cubic (*fcc*) fluorite-type ceria phase (PDF 00-034-0394) in bare CeO$_2$ support and Ni/CeO$_2$ catalysts. The average CeO$_2$ crystallite size of 11 nm was calculated by the Scherrer equation for bare CeO$_2$-R, and this value remained identical after deposition of nickel. No diffraction lines belonging to NiO or metallic nickel were observed in any of the samples, suggesting its presence in the form of small nanoparticles.

TEM analysis of bare CeO$_2$-R support (Fig. 1A and B) and 2Ni catalyst (Fig. 1D and E) confirmed the presence of ceria in the shape of nanorods, which are about 8–15 nm thick and 100–200 nm long. The CeO$_2$ nanorod morphology is dominated by (111) facets, with (100) and (110) facets exposed only at the tips of the nanorods, contributing less than 10% to the overall surface area. Phase identification of fluorite-type
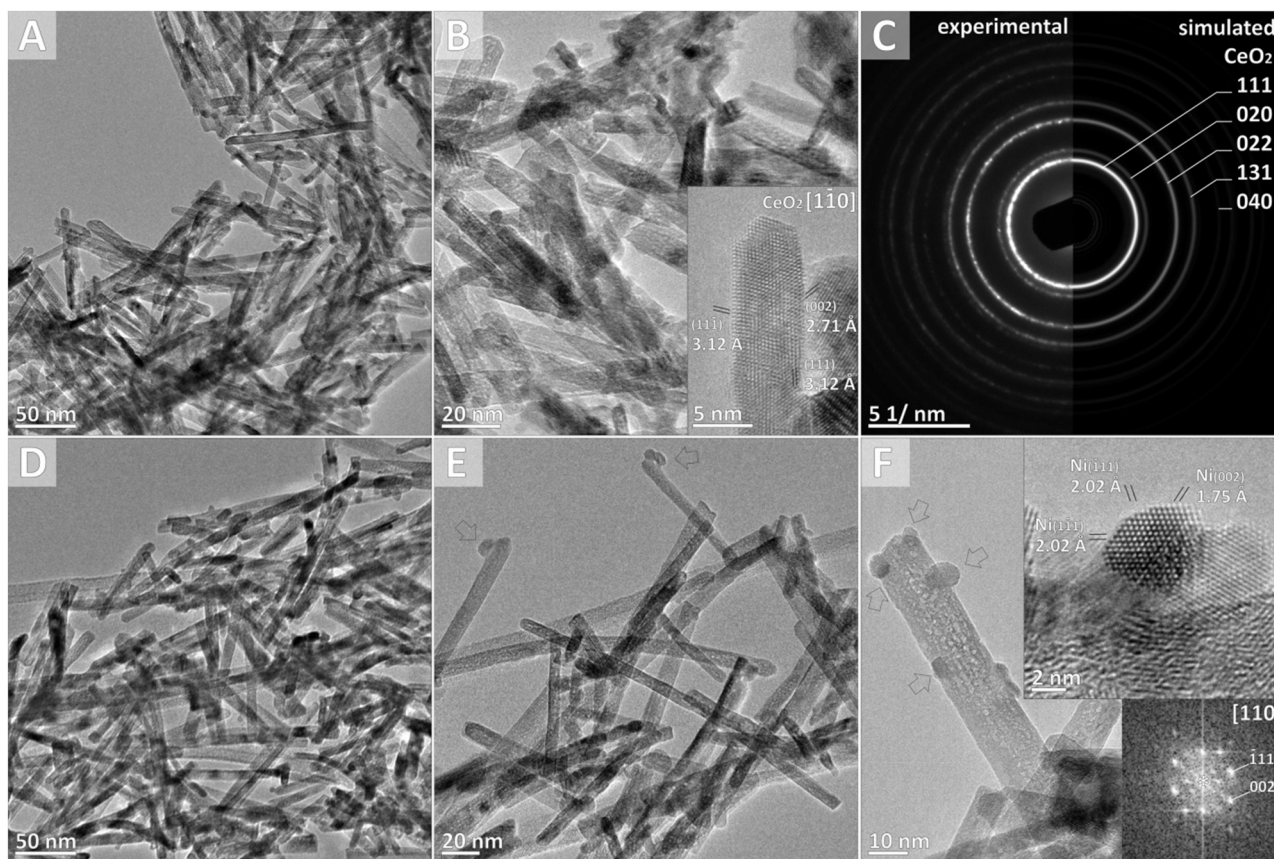

Fig. 1. TEM micrographs of bare CeO$_2$-R support (A, B) and 2Ni catalyst (D–F). The ceria nanorods are crystalline, showing well-developed crystal faces (B, inset). Experimental SAED pattern, recorded over multiple particles, corresponds to pure CeO$_2$ phase with *Fm-3m* (No. 225) space group (C). After Ni deposition, the shape and morphology of nanorods are preserved (D, E), with surface-attached nanoparticles marked by arrows (E); the fast Fourier transform (FFT), calculated from phase-contrast HR-TEM micrograph (F, inset) corresponds to cubic Ni phase with *Fm-3m* (No. 225) space group.

CeO_2 was confirmed by SAED (Fig. 1C). In the 2Ni catalyst sample, nickel was visualized as polyhedral nanoparticles decorating the surface of ceria nanorods (Fig. 1E and F). Nickel particle size, measured from the HR-TEM micrographs, range between 5.1 and 6.5 nm, matching the values obtained by the H_2 chemisorption-TPD technique (Table S2).

The redox properties of CeO_2 are indicative of a reversible generation of oxygen vacancies and Ce^{3+} sites, which serve as active sites for dissociative CO_2 adsorption [8,13]. The reducibility of CeO_2 depends on the shape of its crystals, their size and thermal history, and governs on time coke gasification during DRM, which prevents catalyst deactivation [8,12,13]. For the photocatalytic application of ceria, the existence of Ce^{3+} ensures the occupation of energy levels in the 4f orbital. The 4f orbital lies inside the bandgap of ceria, making electron promotion from the 4f orbital to the conduction band achievable by visible light photons [27].

During H_2-TPR analysis of Ni/CeO_2 catalysts (Fig. S6), the reduction started already at 30 °C, whereas for bare CeO_2 nanorods, it was initiated much later at 250 °C. The H_2 consumed during reduction increased progressively with nickel content in the catalysts (Table S2). Based on the quantification of H_2 consumed until 550 °C, 17% of Ce^{4+} was reduced to Ce^{3+} in bare CeO_2-R, and this value was very similar also for 1Ni and 2Ni catalysts (19% and 17%, respectively, Table S2), and decreased to 9% in 4Ni sample. To summarize, the Ni/CeO_2 catalysts contain a notable fraction of reduced Ce^{3+} sites in reducing atmosphere and in the temperature range relevant for catalytic reactions performed in this work.

The *in-situ* UV-Vis DRS was used to analyze the ability of the Ni/CeO_{2-x} catalysts to absorb visible light, which is a prerequisite for photocatalytic activity. The optical bandgap of pristine CeO_2 and Ni/CeO_2 catalysts at 25 °C in air decreased slightly, from 3.21 to 3.12 eV with increasing Ni content from 0 to 4 wt% (Figs. 2, S7 and S8). Upon heating the samples in a 5% H_2/N_2 atmosphere to 450 °C, the bandgap values of Ni/CeO_{2-x} samples decreased to values between 2.92 and 2.79 eV (Fig. 2), making them suitable for visible light harvesting. The thermal contribution to bandgap narrowing is proportional to Boltzmann constant multiplied by the temperature change (8.617×10^{-5} eV/K • ΔT) and is equal for all samples: 0.015 and 0.037 eV when heated from 25 to 200 and 450 °C, respectively. The observed bandgap narrowing is larger (0.21 eV for bare CeO_2 and 0.33 eV for 4Ni when heated in reducing atmosphere from 25 to 450 °C, Fig. 2), revealing the change is dominated by chemical alteration (reduction) of the catalysts. The partial reduction caused a gradual change of color from pale brown to dark grey, resulting in a strong absorption throughout the visible range spectrum (Fig. S7). This sub-bandgap absorption was observed as a

broad peak centered between 500 and 600 nm for all Ni/CeO_{2-x} catalysts in reducing atmosphere. In addition to partial reduction of ceria, the contact between Ni nanoparticles and CeO_2 likely causes formation of Ni-O-Ce bonds at their interface. As a result, trace amounts of the new mixed oxide phase could be formed, resulting in modification of the electronic band structure of CeO_2, which also contributes to narrowing of bandgap. Increasing the nickel content and temperature in the reductive atmosphere is favorable for both optical bandgap narrowing and increased sub-bandgap absorption of Ni/CeO_{2-x} catalysts.

Simulation of electromagnetic properties of bare CeO_2 nanorods (10×100 nm in size), bare spherical nickel nanoparticles measuring 6 nm and Ni/CeO_{2-x} nanorods is discussed in the following section to gain more insight into the occurring light-matter interactions.

The extinction cross-section as a function of wavelength for oxidized CeO_2 nanorods (Fig. S9) correlates well with the absorbance measurements of bare CeO_2 at 25 °C in air (yellow trace in Fig. S7). Over fully oxidized CeO_2, negligible absorption for wavelengths longer than 400 nm is expected. However, reduced CeO_{2-x} shows remarkable extinction in the visible part of the spectra due to the non-negligible extinction coefficient for energies below the band-gap [33], as was observed experimentally using *in-situ* UV-Vis analysis. We also computed the extinction cross-section of an oxidized CeO_2 rod covered by a thin (1 or 2 nm) external shell of partly reduced ceria (CeO_{2-x}) [34]. Radial concentration gradients of cerium oxidation state (surface enrichment with Ce^{3+}) were previously experimentally observed in CuO/CeO_2 nanorod catalysts [35]. Our simulations showed a strong positive correlation between the thickness of the surface layer containing Ce^{3+} cerium sites and absorbance below the band-gap energy for CeO_{2-x}, expressed as a broad tail. It should be noted that a direct comparison between the optical response of fully reduced (Ce_2O_3) and fully oxidized (CeO_2) ceria is difficult due to the lack of studies correlating oxidation state (exact fraction of Ce^{3+} and Ce^{4+}) and optical properties. In any case, our calculations and *in-situ* experimental data strongly indicate that partial reduction of CeO_2 and presence of Ce^{3+} leads to enhanced sub-band gap absorption.

The extinction cross-section of a bare 6 nm metallic nickel nanosphere is moderate when illuminated by wavelengths between 250 and 800 nm. (Fig. S10A.) The plasmon resonance in Ni nanoparticles strongly overlaps with the contribution of bound d electrons and can be hardly discerned in the extinction cross-section [36]. However, the plasmon-related enhancement of electromagnetic field intensity around the nanoparticle surface shows better-resolved features. The near-field response (like near field enhancement, Fig. S10B) of plasmonic nanoparticles is red-shifted with respect to the far-field response (like the extinction cross-section) for systems with significant losses [37]. However, in the case of nickel, the average and maximum near field enhancement is very moderate, making it a poor plasmonic metal.

Simulation of electromagnetic properties of partly reduced CeO_{2-x} rods decorated with one or five spherical 6 nm Ni nanoparticles (Fig. 3A) shows that the presence of Ni nanoparticles does not significantly modify the absorption properties of the partly reduced ceria.

The absorbance of CeO_{2-x} rods is 1–2 orders of magnitude larger than that of bare nickel nanoparticles (Figs. S9 and S10A). Our simulations suggest that the experimentally observed remarkable increase of absorption below the bandgap of CeO_{2-x} does not seem to be related to the presence of Ni nanoparticles. The average field enhancement over the Ni surface in the Ni/CeO_{2-x} system is comparable to the values obtained for individual Ni particles (Figs. 3B and S10B). However, the maximum field enhancement in the region around the contact point between Ni and CeO_{2-x} rod (Fig. 3C) is almost two orders of magnitude larger than the average value over the particle surfaces, thus creating 'hot spots', Fig. 4 [38]. This can have important consequences also for accelerating photocatalytic methane activation. Rodriguez et al. [39]. report that at the interface between nickel and ceria, methane dissociation is strongly promoted through electronic perturbation of nickel, induced by the reduced ceria.
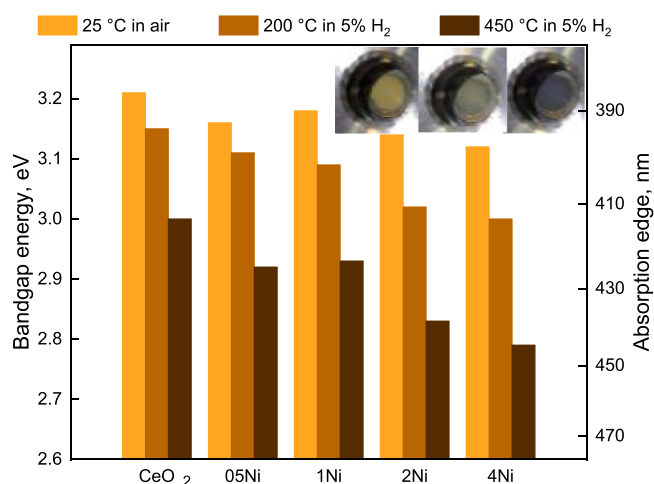

Fig. 2. Bandgap energies for bare CeO_2-R and Ni/CeO_2 catalysts containing 0.5–4 wt% Ni in air at 25 °C and 200 °C and 450 °C in 5% H_2/N_2 atmosphere. Inset shows the 2Ni catalyst at mentioned temperatures and atmospheres.
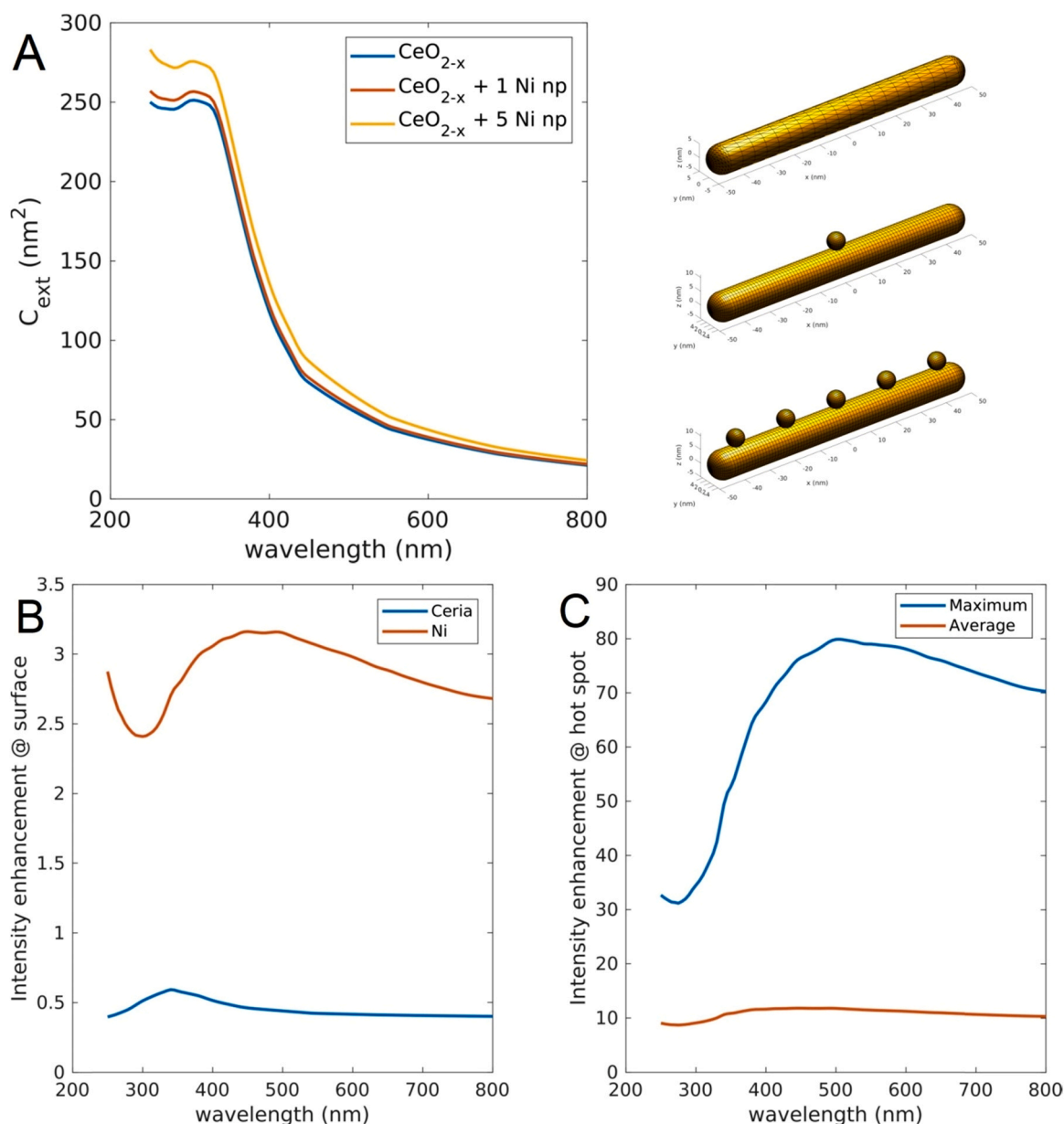
Fig. 3. (A) Extinction cross section of bare CeO_{2-x} rods and decorated with 1 or 5 spherical nickel nanoparticles measuring 6 nm in diameter. Geometric scheme of the simulated structures is shown top right. Near-field intensity enhancements of a CeO_{2-x} nanorod decorated with one spherical nickel nanoparticle: (B) average enhancement calculated over Ni and CeO_{2-x} surfaces and (C) average and maximum enhancement calculated in the hot spot region (cubic volume of 64 nm^3 centered at the contact point between Ni and CeO_{2-x} nanorod).

3.2. Thermally driven and light-assisted catalytic performance

Thermally driven DRM performance of Ni/CeO_{2-x} catalysts is shown in Figs. 5A and S11. No other reaction products were observed beside H_2, CO and water, which is consistent with occurrence of DRM and RWGS reactions. The CH_4 and CO_2 conversion, as well as the H_2/CO ratio, increased with temperature and nickel content in the catalysts (05Ni < 1Ni < 2Ni ≈ 4Ni). Increasing the nickel content accelerates the DRM reaction rate due to the higher number of active sites for methane activation, which is the rate-determining step in the DRM reaction [9, 40]. The H_2/CO ratio and consequently H_2 selectivity increased in parallel with Ni particle size, likely due to the more dominant direct methane dehydrogenation pathway over larger nickel metallic particles. Over smaller Ni clusters, the contribution of the oxygen-assisted methane activation pathway at the nickel-ceria interface, which produces water, is more dominant [41,42]. This is due to oxygen spillover

from the ceria to nickel and a relatively larger fraction of interface perimeter over smaller nickel particles. The amount of accumulated carbon on the catalysts during 6 h of the reaction was very low (0.1–0.2 wt%) for 05Ni, 1Ni and 2Ni samples but increased sharply to 12 wt% on 4Ni catalyst (Table S2). The carbon accumulation rate during the DRM reaction is strongly dependent on nickel particle size and accelerates quickly as nickel size exceeds 5 nm [9,12].

During the light-assisted DRM experiments, the catalysts were constantly illuminated with white light (790 mW cm^{-2}), and the power output of the electric heater was adjusted to vary the catalyst temperature (Figs. 5B and S12). In the light-assisted mode, the 2Ni catalyst was most active, close followed by the 4Ni. The CH_4 and CO_2 conversions were greatly increased compared to the thermocatalytic tests at identical catalyst temperatures. Namely, the light-assisted CH_4 rates over 2Ni catalyst were 4.26 and 1.58 mmol $CH_4/g_{cat} \cdot$ min at 460 and 362 °C, respectively. During thermally-driven catalysis at these exact
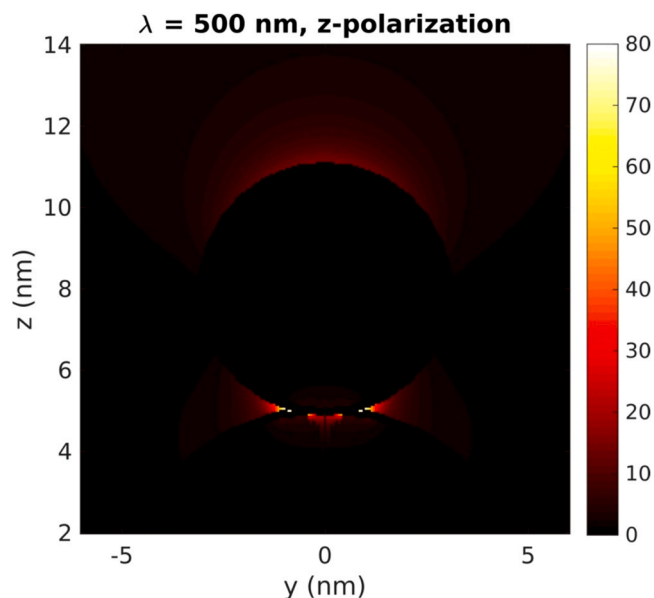
Fig. 4. Spatial distribution of near field intensity enhancement for a Ni/CeO$_{2-x}$ catalyst calculated at the wavelength where largest field enhancement takes place for light polarization parallel to the axis joining the Ni sphere and CeO$_{2-x}$ rod.
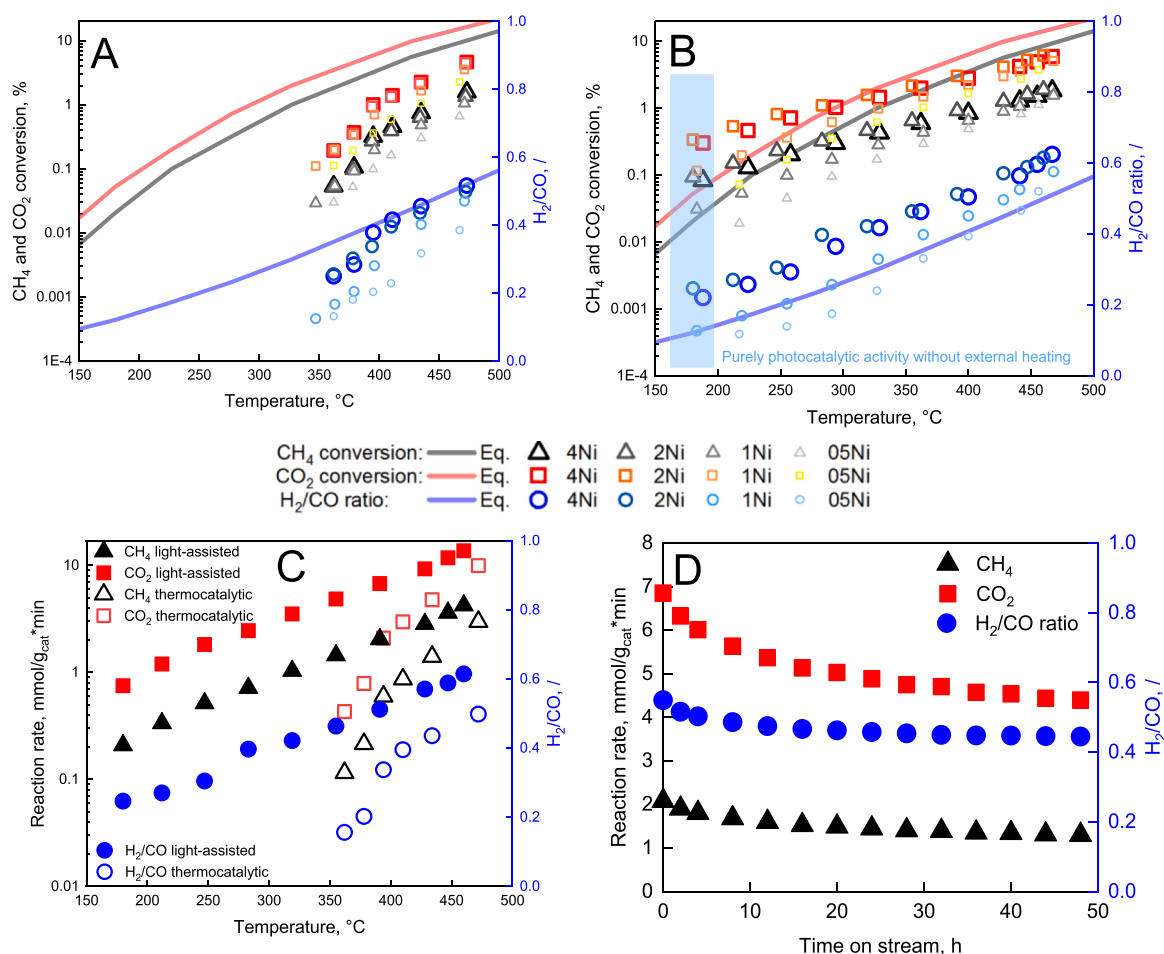
temperatures, the values were 2.48 and 0.097 mmol CH$_4$ (g$_{cat}$ • min)$^{-1}$, respectively (Figs. 5C, S11A and S12A). Regardless of nickel content, no CH$_4$ or CO$_2$ conversion could be identified below 347 °C during thermally driven DRM. However, CH$_4$ and CO$_2$ rates of 0.2 and 0.8 mmol (g$_{cat}$ • min)$^{-1}$ were observed over the 2Ni catalyst in purely photocatalytic mode with no external heating (highlighted by blue rectangle in Fig. 5C). Under such reaction conditions, the 2Ni catalyst temperature was 180 °C. The purely photocatalytic rates over 2Ni catalyst are comparable to those achieved by Shoji et al. [19]. over Rh/SrTiO$_3$ catalyst, irradiated by a 150 W Hg-Xe lamp at 200 °C. A more comprehensive comparison of light-assisted DRM performance is shown in Table 1.

Also, in the light-assisted mode at temperatures up to 250 and 300 °C, respectively (Fig. 5B), the 2Ni and 4Ni catalysts enabled CH$_4$ and CO$_2$ conversions well beyond the values predicted by thermodynamic equilibrium. The photocatalytic activity is limited by the number of photons provided by the light source, whereas the thermocatalytic activity increases exponentially with increasing temperature according to the Arrhenius law [19,20,26]. As a result, the highest photocatalytic gain was observed at low temperatures, where the thermocatalytic rate is slowest.

In the light-assisted mode, the 2Ni catalyst produced syngas with the H$_2$/CO ratio of 0.61 and 0.47 at 460 and 362 °C, respectively. These values are substantially higher than the maximum values predicted by the thermodynamic equilibrium. During thermally-driven reaction at identical catalyst temperatures, the H$_2$/CO ratio was 0.48 and 0.16. Consequently, light-assisted DRM proceeds with higher H$_2$ selectivity

Fig. 5. (A) Conversion of CH$_4$ and CO$_2$, as well as H$_2$/CO ratios produced during thermocatalytic and (B) light-assisted DRM reaction over Ni/CeO$_{2-x}$ nanorod catalysts. Thermodynamic equilibrium values of CH$_4$ and CO$_2$ conversion and H$_2$/CO ratios are shown by full grey, red and blue lines. (C) Comparison of CH$_4$ and CO$_2$ rates and H$_2$/CO ratio produced during light-assisted and thermocatalytic DRM reaction over 2Ni catalyst as a function of catalyst temperature. (D) Long-term light-assisted performance of 2Ni catalyst at 400 °C and constant irradiation by 790 mW/ cm^{-2} of white light.

Table 1
Comparison of light-assisted DRM performance between various catalysts.

Catalyst	Catalyst temperature and feed composition	Irradiance, W/cm^2	CH$_4$ rate, mmol/ g$_{cat}$ • min	H$_2$/CO ratio, /	Source
2% Ni/CeO$_2$	T = 400 °C CH$_4$: CO$_2$ = 1:1	0.79	2.2	0.53	This work
Pd$_{90}$Au$_{10}$/ Al$_2$O$_3$	T = 500 °C CH$_4$: CO$_2$ = 1:1	0.21	0.9	0.9	[23]
5% Ni/Al$_2$O$_3$	T = 300 °C CO$_2$: CH$_4$: Ar = 1: 1: 8	0.25	0.1	0.69	[43]
Ru$_{0.2}$Cu$_{19.8}$/ MgO- Al$_2$O$_3$	T = 727 °C CH$_4$: CO$_2$ = 1:1	19.2	16.5	1	[26]
10% Rh/ SrTiO$_3$	T = ~ 120 °C CH$_4$: CO$_2$: Ar = 1: 1: 98	0.056	0.5	1	[19]
1% Pt/ 0.1SiO$_2$- 0.9CeO$_2$	T = 600 °C CO$_2$: CH$_4$: Ar = 1: 1: 8	3.6	1.5	0.58	[44]
1% Pt/Zn- CeO$_2$	T = 600 °C CO$_2$: CH$_4$: Ar = 1: 1: 8	3.6	2	0.48	[45]
3% Ag-5% La-pCNNT	T = 100 °C CO$_2$: CH$_4$ = 1: 1	0.15	~ 0.03	0.14[a]	[46]
12% Ni/ CeO$_2$	T = ~ 25 °C CH$_4$: CO$_2$: Ar = 0.98: 1: 8.02	0.47	2.6	1	[47]

[a] Methanol and C$_2$H$_6$ were identified among reaction products.

compared to thermocatalytic one at identical catalyst temperatures. The H$_2$ selectivity during DRM is strongly affected by the co-occurring RWGS reaction, and visible light illumination diminishes its contribution to the product selectivity over Ni/CeO$_{2-x}$ catalysts. This is in line with previous findings of Zhou et al. [26], who attributed the 100% H$_2$ selectivity during DRM to visible light stimulating H$_2$ desorption from ruthenium active sites, thus decelerating the RWGS rate. Also, with increasing catalyst temperature, the DRM rate increases faster compared to RWGS rate (Apparent Activation Energy for DRM and RWGS were estimated at 82 and 74 kJ mol^{-1} by Halas et al. [26]. Consequently, by increasing the temperature, a higher H$_2$/CO ratio is expected.

Long-term light-assisted catalytic activity was tested at 400 °C for the most active 2Ni catalyst (Fig. 5D). During the 50 h time on stream, the initial CH$_4$ and CO$_2$ rates decreased by 37% and 35%, and the initial value of H$_2$/CO dropped from 0.55 to 0.44, revealing catalyst deactivation takes place. Analysis of spent 2Ni catalyst identified 1 wt% of carbon on the sample, thus likely excluding active site blocking as a source of deactivation.

The following analysis was applied to exclude the localized sample heating as the source of the photocatalytic effect, observed over the Ni/ CeO$_{2-x}$ catalysts. The apparent activation energies (Ea) in the thermocatalytic mode (90–130 kJ mol^{-1}) decreased to 30–55 kJ mol^{-1} in the light-assisted mode, where excitation by light and thermal energy were supplied in parallel to drive the reaction (inset Figs. S11A and S12A). The apparent activation energy includes the contributions of activation barriers for the rate-determining step (RDS), the enthalpy of the steps that produce species involved in the RDS and a coverage-dependent contribution related to the enthalpy required to regenerate the active sites occupied by reaction intermediates [48]. The decrease of Ea indicates a change in the reaction mechanism related to light-driven methane activation, which occurs in parallel to the thermally-driven mechanism in the light-assisted DRM mode.

Also, we estimated the local temperature increase of the 6 nm nickel particle under constant illumination, as proposed by Baffou [49], which was found to be between 1 and 2 °C. The CH$_4$ rate is accelerated by about 5% when the catalyst temperature increases by 2 °C. However,

over the 2Ni sample, the smallest difference between light-assisted and thermally driven CH$_4$ rates was 71%, in favor of the light-assisted reaction at identical catalyst temperature. Zhou et al. [26] compared the catalyst temperature upon visible light illumination in the same microreactor reactor as used in our work: The values measured by a thermocouple positioned in the catalyst bed and by the thermal camera were identical.

As a control experiment, light-assisted DRM activity was benchmarked to the thermally driven one over the 2Ni/SiO$_2$ catalyst (Fig. S13A). Silica is a wide bandgap insulator, and when coupled with poor visible light absorption of nickel (Fig. S10), negligible photocatalytic activity gain is expected during this experiment. Indeed, the CH$_4$ and CO$_2$ rates differ by less than 5% in thermal and light-assisted DRM experiments at identical catalyst temperatures, revealing the temperature measurement inside the catalyst layer reflects the local temperature at the metallic particles. This experiment also confirmed that the accelerated DRM rate observed over Ni/CeO$_2$ catalysts is related to light absorption by the CeO$_{2-x}$, which agrees with our analysis (Figs. 3, S9, S10 and S13B). However, during the light-assisted DRM over 2Ni/SiO$_2$, the H$_2$/CO ratio was consistently higher compared to the thermocatalytic experiment. This is likely a result of accelerated H$_2$ desorption from the nickel surface *via* desorption induced by electronic transitions (DIET) mechanism [50], which decelerated the RWGS reaction rate. Control experiments with pure CeO$_2$-R support and SiC confirmed their negligible contribution to photocatalytic activity and identified the presence of nickel as crucial for enabling the DRM reaction (Fig. S14). Based on the above control experiments, the observed DRM rate acceleration upon illumination has a photocatalytic, and not thermal origin.

The effect of wavelength on light-assisted DRM activity was tested on the 2Ni catalyst at a constant irradiance of 300 mW cm^{-2} using different bandpass filters (Fig. 6A). The acceleration of CH$_4$ rate was observed for all wavelengths, compared to the thermally-driven methane rate, which equaled 0.49 mmol (g$_{cat}$ • min)$^{-1}$ at identical catalyst temperature. Interestingly, the lowest light assisted CH$_4$ rate (0.61 mmol(g$_{cat}$ • min)$^{-1}$) was observed for illumination with wavelengths shorter than 450 nm, which is the only fraction of light that enables electron promotion from the VB to the CB of CeO$_{2-x}$ and their further migration to nickel nanoparticles, where they can assist in methane activation. The methane rate of 0.62 mmol (g$_{cat}$ • min)$^{-1}$ was achieved during illumination with the lowest energy photons (λ > 600 nm), which can undergo only sub-bandgap electron transitions. The most pronounced rate acceleration was observed with wavelengths between 450 and 550 nm, which correlates with the wavelength dependence of the near-field electromagnetic intensity enhancement on nickel nanoparticles (Fig. 3C).

The effect of irradiance on the CH$_4$ and CO$_2$ rates, as well as H$_2$/CO ratio over the 2Ni catalyst, was probed at the constant catalyst temperature of 395 °C (Fig. 6B). To maintain the catalyst temperature constant with increasing irradiance, the output of the electric heater was decreased simultaneously. The dependence of photocatalytic rate on light intensity (I) reveals plenty about the reaction mechanisms in light-assisted reactions [51]. Four different kinetic categories are classified: sublinear (rate $\propto$ I^n, n < 1), linear (rate $\propto$ I), superlinear (rate $\propto$ I^n, n > 1) and exponential (rate $\propto$ e$^{f(I)}$) [52]. Plasmon-induced photocatalysis has been demonstrated to exhibit each of these regimes, depending on the operating conditions, except for the sublinear dependence, which is characteristic of non-plasmonic semiconductor catalysis when charge carrier recombination is dominant [53]. The exponential dependence is characteristic for thermally driven reactions. Both linear (rate $\propto$ I) and superlinear (rate $\propto$ I^n, n > 1) regimes are distinctive features of electron-driven chemical transformations on metal surfaces, but the reaction conditions are the key factor determining the prevalence of each of them [51].

The acceleration of CH$_4$ and CO$_2$ rates, as well as H$_2$/CO ratio, started to increase notably as irradiance exceeded 400 mW cm^{-2}. At
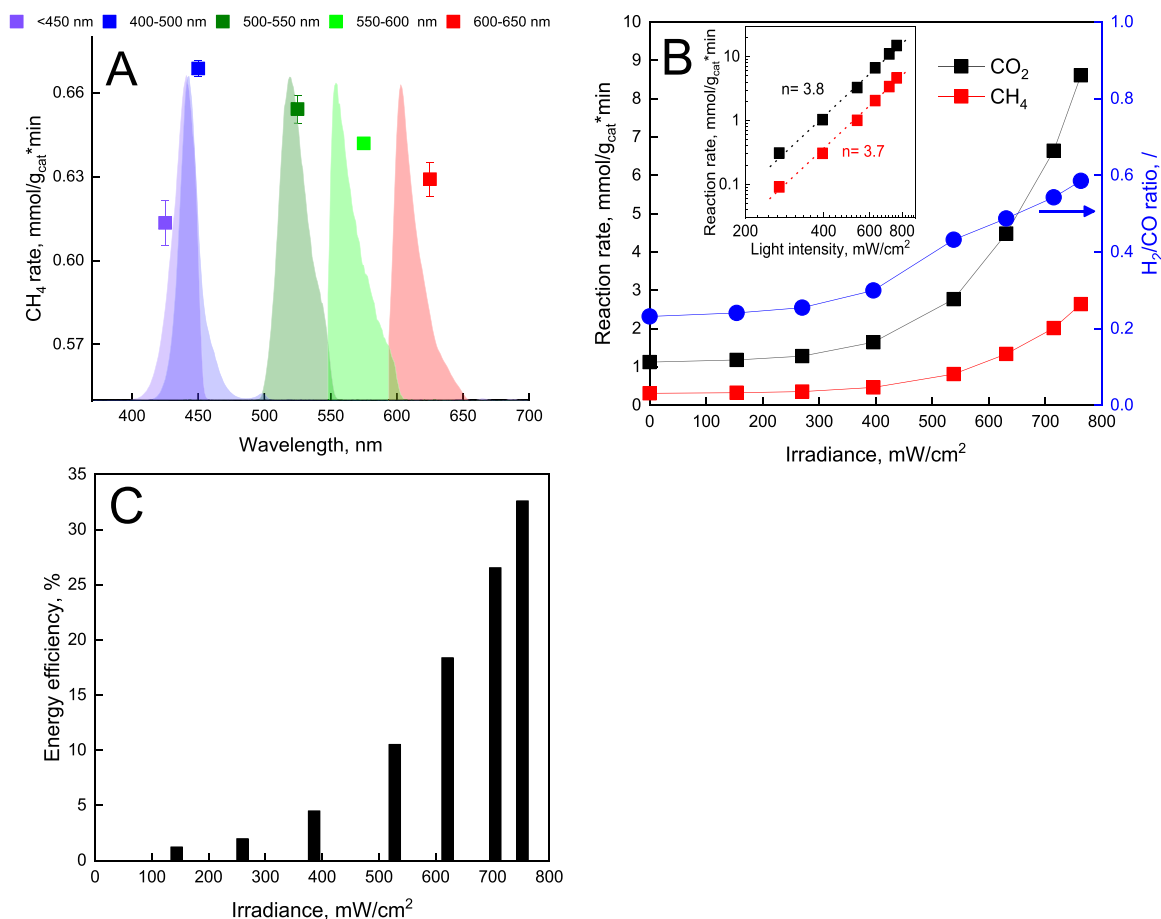
Fig. 6. (A) The CH_4 rate as a function of wavelength at a constant irradiance of 300 mW cm^{-2} and constant catalyst temperature of 395 °C. Colored cones show light intensity dependence on wavelength when using different bandpass filters. (B) CH_4 and CO_2 rate with corresponding H_2/CO ratio as a function of irradiance at a constant catalyst temperature of 400 °C. (C) Energy efficiency related to the experiment shown in panel B.

790 mW cm^{-2}, the CH_4 and CO_2 rates were accelerated by 852% and 769% compared to the thermocatalytic experiment in the dark at identical catalyst temperature, and the H_2/CO ratio increased from 0.23 to 0.59. The inset in Fig. 6B shows the superlinear dependence of both CH_4 and CO_2 rates on irradiance over 2Ni/CO_{2-x} catalysts. This again points to a conclusion that electron-driven chemical transformations on metal surfaces, and not thermal energy are responsible for rate acceleration.

The calculated energy efficiency (Fig. 6C) increased rapidly at irradiances above 400 mW/cm^{-2} and reached 33% at 790 mW cm^{-2}. This revealed the 2Ni as an efficient photocatalyst for visible light utilization.

Hot carriers, generated by plasmon decay in the nickel nanoparticles were analyzed by DFT, as they could alter the reaction pathway of methane dissociation. Initial hot carrier probability distribution can be obtained from calculated density of states (DOS, see Supplementary information and Fig. S15) for photoexcitation with energy E_{ph} and Fermi distribution at room temperature. Probability distributions for hot carrier generation suggest that for photon energies corresponding to visible light (up to 3.26 eV or 380 nm), nickel should not be an efficient source of hot carriers, Fig. S16.

Cumulative hot carrier generation probability (Fig. S17) shows that the trend for hot carrier generation increases gradually and almost linearly with the increasing photon energy in the visible range, after which it sharply increases in the UV range. In contrast, the experimental data in Fig. 6A shows a sharp decrease of reaction rate below 450 nm (above 2.76 eV). Had the reaction been catalyzed by hot carriers generated in Ni nanoparticles, the reaction rate would be expected to follow the trend of hot carrier generation probability and continue increasing as the

wavelength gets shorter. It has to be noted that hot carrier generation probability is an intrinsic property of the material and the near-field intensity could change the absolute number of generated hot carriers and, consequently, the rate of reaction catalyzed by hot carriers. The aforementioned moderate hot carrier generation probability in the spectral range where the experiments were carried out, diverging trends in generation probability and reaction rate as the photon energy approaches UV range, and low near-field intensity enhancement inside Ni nanoparticles suggest that hot carriers are unlikely to be generated in Ni nanoparticles.

4. Discussion

Based on the characterization, theoretical and catalytic data, we can postulate the light-assisted DRM mechanism over the Ni/CeO_{2-x} catalyst. First, we discuss the situation where the catalyst is irradiated with photons having energy higher than its bandgap (hot-carrier mediated photocatalytic mechanism, Fig. 7A).

During DRM reaction, nickel is present as metallic nanoparticles [8] measuring about 5 nm and ceria as a partly reduced (CeO_{2-x}) semiconductor [8]. Ceria is an n-type semiconductor whose work function (5.34 eV) is larger than that of nickel (5.01 eV) [54]. After illuminating the Ni/CeO_{2-x} catalysts with photons having energy higher than 2.84 eV, (the absorption edge of 2Ni-R was estimated at ~ 440 nm, Fig. 2), the photo-excited electrons migrate from the 4f orbital of CeO_{2-x} to its conduction band, and are transferred to nickel. An upward band bending in the n-type semiconductor is created due to the accumulation of excess positive charge in the semiconductor caused by electron
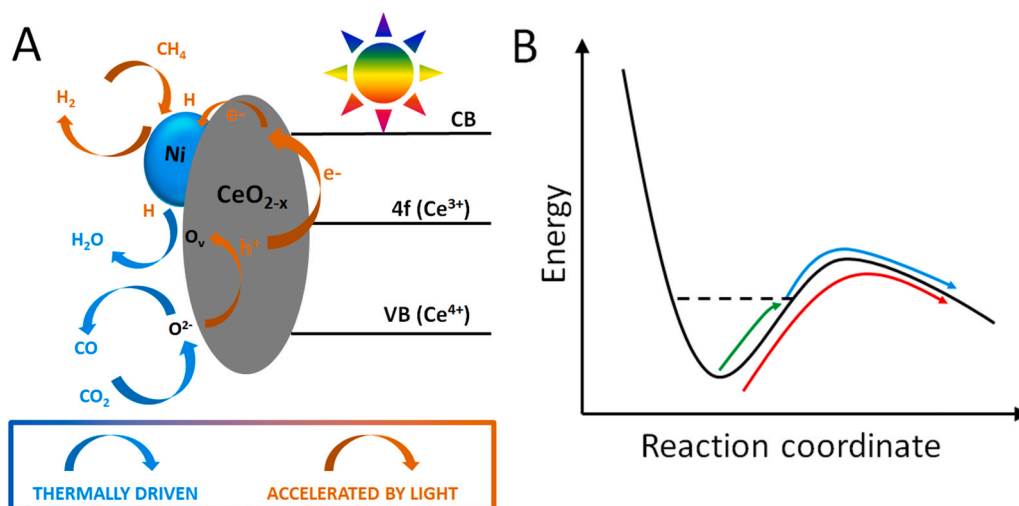
Fig. 7. A) Schematic representation of the hot-carrier driven photocatalytic mechanism on the Ni/CeO$_{2-x}$ catalyst and B) alleviation of the energy barriers due to near field electromagnetic enhancement energy transfer.

migration. As a result, a Schottky barrier is created, which serves as an electron trap, leading to electron accumulation on the nickel and prevents their migration back to the semiconductor. The hot electrons on nickel can be transferred to the LUMO of adsorbed methane and electronically excite the CH$_x$ species, thus accelerating C—H bond cleavage (orange arrows in Fig. 7A). Hot electrons can also participate in H$^+$ and e$^-$ recombination, leading to accelerated formation and desorption of molecular H$_2$. This should result in higher abundance of free nickel sites where activation of adsorbed methane molecules can occur, resulting in accelerated methane activation and overall increase of DRM rate (considering methane activation is the RDS of reaction).

The role of light on the photocatalytic CO$_2$ reaction pathway was tested with the 2Ni catalyst in the light-assisted RWGS reaction (CO$_2$ + H$_2$ ↔ CO + H$_2$O). The concentrations of H$_2$ and CO$_2$ were very similar to the values measured during the DRM test (Fig. S18). The RWGS reaction is rate-determined by the dissociation of CO$_2$, which takes place over partly reduced CeO$_2$ [55]. The H$_2$ dissociation is much faster and occurs over nickel with a low activation barrier (0.1 eV for Ni [111]). Since H$_2$ activation on nickel is kinetically fast, its acceleration should have a minor role on the RWGS rate, as CO$_2$ activation is the step which controls the overall RWGS reaction rate.

During progressively increasing irradiance from 0 to 790 mW cm^{-2} (and a simultaneous decrease of thermal energy input, resulting in constant catalyst temperature of 400 °C), the CO rate increased by 11%. During the DRM reaction at identical reaction conditions, CH$_4$ rate increased by 852% (Fig. 6B). Thus, the very different response of the Ni/CeO$_{2-x}$ catalyst during light-assisted RWGS and DRM reactions suggests that visible light does not play any meaningful role in accelerating CO$_2$ dissociation under tested reaction conditions. However, it strongly accelerates CH$_4$ dissociation over nickel.

Our experimental findings are in accordance with those of Zhang et al. [47]. who used DFT to analyze the energetics of elementary reaction steps on nickel in ground and excited state (simulating illumination). They observed no decrease in activation barriers in the CO$_2$ reaction pathway, whereas activation barriers for the CH dissociation and oxidation of C and CH species, leading to accelerated DRM rates.

Based on the above, we can postulate that CO$_2$ activation on partly reduced ceria during DRM under reaction conditions studied is exclusively thermally driven, whereas methane activation over nickel is a light-assisted process. One has to keep in mind that methane activation is the rate determining step of the DRM reaction and the (photocatalytic) DRM rate acceleration will be noticed until the methane dissociation catches up with the CO$_2$ dissociation rate.

The catalytic role of hot holes (h$^+$), accumulated on CeO$_{2-x}$ is more

difficult to establish. The *in-situ* DRIFTS is a powerful surface characterization tool and was used to analyze CO$_2$ activation over the 2Ni catalyst in thermally-driven and light-assisted modes (see Supplementary information for more details, Fig. S19). The characteristic bands of carbonates are analyzed, which populate exclusively the ceria surface. The mono- and bidentate carbonates are the active intermediates in the CO$_2$ activation and dissociation pathway, whereas polydentate is an inert spectator at temperatures below 500 °C.

The surface carbonates on oxidized 2Ni sample in dark (Fig. S19A) are present mainly as polydentate (1454 cm^{-1}), accompanied by some monodentate (1588 cm^{-1}) and bidentate carbonate species (1282 cm^{-1}). Upon illumination, no change occurs in the polydentate carbonate band and a very modest change in the mono and bidentate.

Contrary, over the reduced 2Ni catalyst in dark (Fig. S19B), the carbonate distribution is very different. The monodentate and bidentate prevail over the polydentate, indicating strongly altered CO$_2$ adsorption sites, compared to the oxidized sample. Catalyst illumination induces a drastic decrease of the monodentate and bidentate carbonate coverage, and simultaneously increases the polydentate band intensity.

Finally, the carbonate DRIFT spectra of the reduced 2Ni sample in H$_2$/CO$_2$ atmosphere in dark (Fig. S19C) show dominant monodentate vibrations (due to more abundant Ce^{3+} at 400 °C in H$_2$/CO$_2$ flow, compared to CO$_2$ flow, Fig. S19B), which are attenuated upon illumination, with a concomitant rise of the polydentate band. The monodentate band decrease is less pronounced compared to the one in pure CO$_2$ flow (Fig. S19B and C), as H$_2$ atmosphere maintains a higher fraction of Ce^{3+}.

Based on the similarity between carbonate bands of oxidized 2Ni, and reduced illuminated 2Ni catalysts, oxidation of ceria can be assumed to occur during illumination.

Upon illumination of the Ni/CeO$_{2-x}$ catalyst, the electron is excited from the 4f orbital of Ce^{3+} to the conduction band and migrates to nickel, causing h$^+$ accumulation on ceria. Hot holes can participate in the reaction with surface adsorbed oxide species (O^{2-}) originating from CO$_2$, and fill the oxygen vacancy sites, causing ceria re-oxidation. This process should not be mistaken with CO$_2$ activation, which is driven by electron transfer [56] from electron rich Ce^{3+} sites to the adsorbed CO$_2$, producing CO$_2^-$. The electron transfer process is the rate-limiting step for CO$_2$ splitting over ceria based materials at moderate temperatures [57].

The light-assisted rate acceleration does not correlate with decreasing wavelength (increasing photon energy), which is expected for the hot-carrier driven mechanism. This suggests the existence of an additional light-driven reaction mechanism, which is depicted in Fig. 7B (shown for ground state when the catalyst is illuminated by photons

having energy lower than the CeO_{2-x} bandgap). Namely, photons with a shorter wavelength can excite electrons to higher energy levels in the conduction band (CB), increasing the over-potential for charge carriers and thus increasing their reactivity. Furthermore, the methane rate, achieved by illuminating with photons having substantially lower energy than what is required for VB to CB transition in ceria, is higher compared to the methane rate achieved by photons with sufficient energy that enable bandgap transitions (Fig. 6A). The near-field electromagnetic enhancement is strongly dependent on the illumination wavelength and reaches a maximum at about 500 nm (Fig. 3C). Upon illuminating the 2Ni catalyst with 300 mW cm^{-2} of light using a band-pass filter transparent for wavelengths between 500 and 550 nm, a methane rate of 0.65 mmol $(g_{cat} \bullet min)^{-1}$ was achieved which represents a 33% increase compared to the experiment in the dark. The localized near field enhancement induces resonant energy transfer into the Ni-CH$_x$ bond (green arrow in Fig. 7B). As the vibrational energy stored in the bond increases, it gets progressively more destabilized [58]. As a result, the energy barrier which remains to be overcome by thermal energy (blue arrow in Fig. 7B) is lowered, which manifests as lower apparent activation energy (inset Figs. S11A and S12A) and accelerated DRM rate. In the thermally-driven mode (red arrow in Fig. 7B), the activation barrier remains high because thermal energy is the only means of activation of adsorbed reaction intermediates, which drives the catalytic reaction.

5. Conclusions

This work analyzes the underlying mechanism of visible light assisted DRM rate acceleration over Ni/CeO$_{2-x}$ catalysts. The *in-situ* UV-Vis analysis and simulation of electromagnetic properties revealed that the presence of Ce^{3+} in partly reduced ceria is crucial for visible light absorption. The light-assisted DRM test showed that methane and CO$_2$ rates, as well as hydrogen selectivity, are greatly improved compared to thermally driven experiments at identical catalyst temperatures. Two weight percent nickel was found as optimal active metal loading, enabling high (photocatalytic) reaction rates, energy efficiency of 33% and minimal carbon accumulation. Photocatalytic DRM activity is maintained over the 2Ni catalyst in purely photocatalytic mode with 790 mW cm^{-2} of white light irradiance and without external heating. Simulation of electromagnetic properties identified the electromagnetic near field intensity enhancement occurs mainly over nickel nanoparticles, which are the active sites for methane activation. The light assisted DRM rate is wavelength dependent and reaches a maximum at about 500 nm, which also triggers the highest near field enhancement. Two mechanisms exist simultaneously during white light illumination: hot carrier driven charge transfer, employing photons with energy higher than the bandgap of partly reduced ceria and near field enhancement induced resonant energy transfer, concentrated over the nickel-ceria interphase, stimulated by sub- bandgap absorption of low energy photons. This work can act as a cornerstone for further developing Ni/CeO$_2$ based catalysts for visible light-driven methane activation under mild conditions.

CRediT authorship contribution statement

Kristijan Lorber: Investigation, Writing – original draft. **Janez Zavašnik:** Investigation, Formal analysis, Writing – review & editing. **Jordi Sancho-Parramon:** Formal analysis, Writing – review & editing. **Matej Bubaš:** Formal analysis, Writing – review & editing. **Matjaž Mazaj:** Investigation. **Petar Djinović:** Conceptualization, Supervision, Resources, Writing – review & editing, Funding acquisition.

Declaration of Competing Interest

The authors declare that they have no known competing financial interests or personal relationships that could have appeared to influence the work reported in this paper.

Appendix A. Supplementary material

Supplementary data associated with this article can be found in the online version at doi:10.1016/j.apcatb.2021.120745.

References

[1] S. Saeidi, N.A.S. Amin, M.R. Rahimpour, Hydrogenation of CO₂ to value-added products—a review and potential future developments, J. CO₂ Util. 5 (2014) 66–81, https://doi.org/10.1016/j.jcou.2013.12.005.

[2] K. Chang, H. Zhang, M. Cheng, Q. Lu, Application of ceria in CO₂ conversion catalysis, ACS Catal. 10 (2020) 613–631, https://doi.org/10.1021/acscatal.9b03935.

[3] A.A. Khan, M. Tahir, Well-designed 2D/2D Ti₃C₂T$_{A/R}$ MXene coupled g-C₃N₄ heterojunction with in-situ growth of anatase/rutile TiO₂ nucleates to boost photocatalytic dry-reforming of methane (DRM) for syngas production under visible light, Appl. Catal. B: Environ. 285 (2021) 119777, https://doi.org/10.1016/j.apcatb.2020.119777.

[4] A. Indarto, J. Palgunadi, Syngas: Production, Applications and Environmental Impact, Nova Science Publishers, Inc, 2013.

[5] D. Pakhare, J. Spivey, A review of dry (CO₂) reforming of methane over noble metal catalysts, Chem. Soc. Rev. 43 (2014) 7813–7837, https://doi.org/10.1039/C3CS60395D.

[6] R. Horn, R. Schlögl, Methane activation by heterogeneous catalysis, Catal. Lett. 145 (2015) 23–39, https://doi.org/10.1007/s10562-014-1417-z.

[7] P.G. Lustemberg, P.J. Ramírez, Z. Liu, R.A. Gutiérrez, D.G. Grinter, J. Carrasco, S. D. Senanayake, J.A. Rodriguez, M.V. Ganduglia-Pirovano, Room-temperature activation of methane and dry reforming with CO₂ on Ni-CeO₂ (111) surfaces: effect of Ce³⁺ sites and metal–support interactions on C—H bond cleavage, ACS Catal. 6 (2016) 8184–8191, https://doi.org/10.1021/acscatal.6b02360.

[8] F. Zhang, Z. Liu, X. Chen, N. Rui, L.E. Betancourt, L. Lin, W. Xu, C.-J. Sun, A.M. M. Abeykoon, J.A. Rodriguez, K. Lorber, J. Teržan, P. Djinović, S.D. Senanayake, AP-XPS! Effects doping ceriadry reforming methane Ni/CeZrO₂ catalysts: in situ studies, ACS Catal. 10 (2020) 3274–3284, https://doi.org/10.1021/acscatal.9b04451 (acscatal.9b04451).

[9] C. Vogt, J. Kranenborg, M. Monai, B.M. Weckhuysen, Structure sensitivity in steam and dry methane reforming over nickel: activity and carbon formation, ACS Catal. 10 (2020) 1428–1438, https://doi.org/10.1021/acscatal.9b04193.

[10] A. Trovarelli, Catalysis by Ceria and Related Materials, Imperial College Press, 2002, https://doi.org/10.1142/p249.

[11] P. Djinović, I.G. Osojnik Črnivec, B. Erjavec, A. Pintar, Influence of active metal loading and oxygen mobility on coke-free dry reforming of Ni–Co bimetallic catalysts, Appl. Catal. B Environ. 125 (2012) 259–270, https://doi.org/10.1016/j.apcatb.2012.05.049.

[12] P. Djinović, A. Pintar, Stable and selective syngas production from dry CH₄-CO₂ streams over supported bimetallic transition metal catalysts, Appl. Catal. B Environ. 206 (2017) 675–682, https://doi.org/10.1016/j.apcatb.2017.01.064.

[13] A. Trovarelli, J. Llorca, Ceria catalysts at nanoscale: how do crystal shapes shape catalysis? ACS Catal. 7 (2017) 4716–4735, https://doi.org/10.1021/acscatal.7b01246.

[14] K. Chang, H. Zhang, M. Cheng, Q. Lu, Application of ceria in CO₂ conversion catalysis, ACS Catal. 10 (2020) 613–631, https://doi.org/10.1021/acscatal.9b03935.

[15] X. Du, D. Zhang, L. Shi, R. Gao, J. Zhang, Morphology dependence of catalytic properties of Ni/CeO₂ nanostructures for carbon dioxide reforming of methane, J. Phys. Chem. C 116 (2012) 10009–10016, https://doi.org/10.1021/jp300543r.

[16] G. Palmisano, V. Augugliaro, M. Pagliaro, L. Palmisano, Photocatalysis: a promising route for 21st century organic chemistry, Chem. Commun. (2007) 3425–3437, https://doi.org/10.1039/b700395c.

[17] Ştefan Neaţu, J. Maciá-Agulló, H. Garcia, Solar light photocatalytic CO₂ reduction: general considerations and selected bench-mark photocatalysts, Int. J. Mol. Sci. 15 (2014) 5246–5262, https://doi.org/10.3390/ijms15045246.

[18] L. Chen, J. Tang, L.-N. Song, P. Chen, J. He, C.-T. Au, S.-F. Yin, Heterogeneous photocatalysis for selective oxidation of alcohols and hydrocarbons, Appl. Catal. B Environ. 242 (2019) 379–388, https://doi.org/10.1016/j.apcatb.2018.10.025.

[19] S. Shoji, X. Peng, A. Yamaguchi, R. Watanabe, C. Fukuhara, Y. Cho, T. Yamamoto, S. Matsumura, M.-W. Yu, S. Ishii, T. Fujita, H. Abe, M. Miyauchi, Photocatalytic

uphill conversion of natural gas beyond the limitation of thermal reaction systems, Nat. Catal. 3 (2020) 148–153, https://doi.org/10.1038/s41929-019-0419-z.

[20] P. Mehta, P.M. Barboun, Y. Engelmann, D.B. Go, A. Bogaerts, W.F. Schneider, J. C. Hicks, Plasma-catalytic ammonia synthesis beyond the equilibrium limit, ACS Catal. 10 (2020) 6726–6734, https://doi.org/10.1021/acscatal.0c00684.

[21] H. Song, X. Meng, T.D. Dao, W. Zhou, H. Liu, L. Shi, H. Zhang, T. Nagao, T. Kako, J. Ye, Light-enhanced carbon dioxide activation and conversion by effective plasmonic coupling effect of Pt and Au nanoparticles, ACS Appl. Mater. Interfaces 10 (2018) 408–416, https://doi.org/10.1021/acsami.7b13043.

[22] B. Han, W. Wei, L. Chang, P. Cheng, Y.H. Hu, Efficient visible light photocatalytic CO₂ reforming of CH₄, ACS Catal. 6 (2016) 494–497, https://doi.org/10.1021/acscatal.5b02653.

[23] H. Liu, M. Li, T.D. Dao, Y. Liu, W. Zhou, L. Liu, X. Meng, T. Nagao, J. Ye, Design of PdAu alloy plasmonic nanoparticles for improved catalytic performance in CO₂ reduction with visible light irradiation, Nano Energy 26 (2016) 398–404, https://doi.org/10.1016/j.nanoen.2016.05.045.

[24] Y. Cho, S. Shoji, A. Yamaguchi, T. Hoshina, T. Fujita, H. Abe, M. Miyauchi, Visible-light-driven dry reforming of methane using a semiconductor-supported catalyst, Chem. Commun. 56 (2020) 4611–4614, https://doi.org/10.1039/D0CC00729C.

[25] N. Abdel Karim Aramouni, J. Zeaiter, W. Kwapinski, M.N. Ahmad, Thermodynamic analysis of methane dry reforming: effect of the catalyst particle size on carbon formation, Energy Convers. Manag. 150 (2017) 614–622, https://doi.org/10.1016/j.enconman.2017.08.056.

[26] L. Zhou, J.M.P. Martirez, J. Finzel, C. Zhang, D.F. Swearer, S. Tian, H. Robatjazi, M. Lou, L. Dong, L. Henderson, P. Christopher, E.A. Carter, P. Nordlander, N. J. Halas, Light-driven methane dry reforming with single atomic site antenna-reactor plasmonic photocatalysts, Nat. Energy 5 (2020) 61–70, https://doi.org/10.1038/s41560-019-0517-9.

[27] M.E. Khan, M.M. Khan, M.H. Cho, Ce₃₊-ion, surface oxygen vacancy, and visible light-induced photocatalytic dye degradation and photocapacitive performance of CeO₂-graphene nanostructures, Sci. Rep. 7 (2017) 5928, https://doi.org/10.1038/s41598-017-06139-6.

[28] M. Zabilskiy, P. Djinović, E. Tchernychova, O.P. Tkachenko, L.M. Kustov, A. Pintar, Nanoshaped CuO/CeO₂ materials: effect of the exposed ceria surfaces on catalytic activity in N₂O decomposition reaction, ACS Catal. 5 (2015) 5357–5365, https://doi.org/10.1021/acscatal.5b01044.

[29] G. Słowik, M. Greluk, M. Rotko, A. Machocki, Evolution of the structure of unpromoted and potassium-promoted ceria-supported nickel catalysts in the steam reforming of ethanol, Appl. Catal. B Environ. 221 (2018) 490–509, https://doi.org/10.1016/j.apcatb.2017.09.052.

[30] S. Velu, S. Gangwal, Synthesis of alumina supported nickel nanoparticle catalysts and evaluation of nickel metal dispersions by temperature programmed desorption, Solid State Ion. 177 (2006) 803–811, https://doi.org/10.1016/j.ssi.2006.01.031.

[31] U. Hohenester, A. Trügler, MNPBEM – a Matlab toolbox for the simulation of plasmonic nanoparticles, Comput. Phys. Commun. 183 (2012) 370–381, https://doi.org/10.1016/j.cpc.2011.09.009.

[32] E.D. Palik (Ed.), Handbook of Optical Constants of Solids, Academic press, 1998.

[33] V.M. Wheeler, J.I. Zapata, P.B. Kreider, W. Lipiński, Effect of non-stoichiometry on optical, radiative, and thermal characteristics of ceria undergoing reduction, Opt. Express 26 (2018) 360, https://doi.org/10.1364/OE.26.00A360.

[34] F. Marabelli, P. Wachter, Covalent insulator CeO₂: optical reflectivity measurements, Phys. Rev. B 36 (1987) 1238–1243, https://doi.org/10.1103/PhysRevB.36.1238.

[35] M. Zabilskiy, P. Djinović, E. Tchernychova, A. Pintar, N₂O decomposition over CuO/CeO₂ catalyst: new insights into reaction mechanism and inhibiting action of H₂O and NO by operando techniques, Appl. Catal. B Environ. 197 (2016) 146–158, https://doi.org/10.1016/j.apcatb.2016.02.024.

[36] H. Amekura, Y. Takeda, N. Kishimoto, Criteria for surface plasmon resonance energy of metal nanoparticles in silica glass, Nucl. Instrum. Methods Phys. Res. Sect. B Beam Interact. Mater. Atoms 222 (2004) 96–104, https://doi.org/10.1016/j.nimb.2004.01.003.

[37] J. Zuloaga, P. Nordlander, On the energy shift between near-field and far-field peak intensities in localized plasmon systems, Nano Lett. 11 (2011) 1280–1283, https://doi.org/10.1021/nl1043242.

[38] S. Sergiienko, K. Moor, K. Gudun, Z. Yelemessova, R. Bukasov, Nanoparticle–nanoparticle vs. nanoparticle–substrate hot spot contributions to the SERS signal: studying Raman labelled monomers, dimers and trimers, Phys. Chem. Chem. Phys. 19 (2017) 4478–4487, https://doi.org/10.1039/C6CP08254H.

[39] Z. Liu, D.C. Grinter, P.G. Lustemberg, T.-D. Nguyen-Phan, Y. Zhou, S. Luo, I. Waluyo, E.J. Crumlin, D.J. Stacchiola, J. Zhou, J. Carrasco, H.F. Busnengo, M.

V. Ganduglia-Pirovano, S.D. Senanayake, J.A. Rodriguez, Dry reforming of methane on a highly-active Ni-CeO₂ catalyst: effects of metal-support interactions on C—H bond breaking, Angew. Chem. Int. Ed. 55 (2016) 7455–7459, https://doi.org/10.1002/anie.201602489.

[40] J. Wei, E. Iglesia, Isotopic and kinetic assessment of the mechanism of reactions of CH₄ with CO₂ or H₂O to form synthesis gas and carbon on nickel catalysts, J. Catal. 224 (2004) 370–383, https://doi.org/10.1016/j.jcat.2004.02.032.

[41] Z. Xie, Q. Liao, M. Liu, Z. Yang, L. Zhang, Micro-kinetic modeling study of dry reforming of methane over the Ni-based catalyst, Energy Convers. Manag. 153 (2017) 526–537, https://doi.org/10.1016/j.enconman.2017.10.022.

[42] K. Yuan, J.-Q. Zhong, X. Zhou, L. Xu, S.L. Bergman, K. Wu, G.Q. Xu, S.L. Bernasek, H.X. Li, W. Chen, Dynamic oxygen on surface: catalytic intermediate and coking barrier in the modeled CO₂ reforming of CH₄ on Ni (111), ACS Catal. 6 (2016) 4330–4339, https://doi.org/10.1021/acscatal.6b00357.

[43] D. Takami, Y. Ito, S. Kawaharasaki, A. Yamamoto, H. Yoshida, Low temperature dry reforming of methane over plasmonic Ni photocatalysts under visible light irradiation, Sustain. Energy Fuels 3 (2019) 2968–2971, https://doi.org/10.1039/C9SE00206E.

[44] F. Pan, X. Xiang, W. Deng, H. Zhao, X. Feng, Y. Li, A novel photo-thermochemical approach for enhanced carbon dioxide reforming of methane, ChemCatChem 10 (2018) 940–945, https://doi.org/10.1002/cctc.201701565.

[45] F. Pan, X. Xiang, Z. Du, E. Sarnello, T. Li, Y. Li, Integrating photocatalysis and thermocatalysis to enable efficient CO₂ reforming of methane on Pt supported CeO₂ with Zn doping and atomic layer deposited MgO overcoating, Appl. Catal. B: Environ. 260 (2020), 118189, https://doi.org/10.1016/j.apcatb.2019.118189.

[46] B. Tahir, M. Tahir, N.A.S. Amin, Ag-La loaded protonated carbon nitrides nanotubes (pCNNT) with improved charge separation in a monolithic honeycomb photoreactor for enhanced bireforming of methane (BRM) to fuels, Appl. Catal. B Environ. 248 (2019) 167–183, https://doi.org/10.1016/j.apcatb.2019.01.076.

[47] Q. Zhang, M. Mao, Y. Li, Y. Yang, H. Huang, Z. Jiang, Q. Hu, S. Wu, X. Zhao, Novel photoactivation promoted light-driven CO₂ reduction by CH₄ on Ni/CeO₂ nanocomposite with high light-to-fuel efficiency and enhanced stability, Appl. Catal. B Environ. 239 (2018) 555–564, https://doi.org/10.1016/j.apcatb.2018.08.052.

[48] H. Lynggaard, A. Andreasen, C. Stegelmann, P. Stoltze, Analysis of simple kinetic models in heterogeneous catalysis, Prog. Surf. Sci. 77 (2004) 71–137, https://doi.org/10.1016/j.progsurf.2004.09.001.

[49] G. Baffou, H. Rigneault, Femtosecond-pulsed optical heating of gold nanoparticles, Phys. Rev. B 84 (2011), 035415, https://doi.org/10.1103/PhysRevB.84.035415.

[50] V.N. Ageev, Desorption induced by electronic transitions, Prog. Surf. Sci. 47 (1994) 55–203, https://doi.org/10.1016/0079-6816(94)90014-0.

[51] D. Mateo, J.L. Cerrillo, S. Durini, J. Gascon, Fundamentals and applications of photo-thermal catalysis, Chem. Soc. Rev. 50 (2021) 2173–2210, https://doi.org/10.1039/d0cs00357c.

[52] M.J. Kale, T. Avanesian, P. Christopher, Direct photocatalysis by plasmonic nanostructures, ACS Catal. 4 (2014) 116–128, https://doi.org/10.1021/cs400993w.

[53] A. Gellé, T. Jin, L. de la Garza, G.D. Price, L.V. Besteiro, A. Moores, Applications of plasmon-enhanced nanocatalysis to organic transformations, Chem. Rev. 120 (2020) 986–1041, https://doi.org/10.1021/acs.chemrev.9b00187.

[54] K. Zhao, J. Qi, Z. Wang, J. Zhao, X. Ma, J. Wan, L. Chang, Y. Gao, R. Yu, Z. Tang, Efficient water oxidation under visible light by tuning surface defects on ceria nanorods, J. Mater. Chem. A 3 (2015) 20465–20470, https://doi.org/10.1039/C5TA05817A.

[55] S.K. Wilkinson, L.G.A. Van De Water, B. Miller, M.J.H. Simmons, E.H. Stitt, M. J. Watson, Understanding the generation of methanol synthesis and water gas shift activity over copper-based catalysts – a spatially resolved experimental kinetic study using steady and non-steady state operation under CO/CO₂/H₂ feeds, J. Catal. 337 (2016) 208–220, https://doi.org/10.1016/j.jcat.2016.01.025.

[56] M.B. Ansari, S.-E. Park, Carbon dioxide utilization as a soft oxidant and promoter in catalysis, Energy Environ. Sci. (2012) 9419–9437, https://doi.org/10.1080/09273948.2016.1207785.

[57] Z. Zhao, M. Uddi, N. Tsvetkov, B. Yildiz, A.F. Ghoniem, Enhanced intermediate-temperature CO₂ splitting using nonstoichiometric ceria and ceria–zirconia, Phys. Chem. Chem. Phys. 19 (2017) 25774–25785, https://doi.org/10.1039/C7CP04789D.

[58] L. Zhou, D.F. Swearer, H. Robatjazi, A. Alabastri, P. Christopher, E.A. Carter, P. Nordlander, N.J. Halas, Response to comment on "Quantifying hot carrier and thermal contributions in plasmonic photocatalysis, Science (80-) 364 (2019) 69–72, https://doi.org/10.1126/science.aaw9545.